This CVPR Workshop paper is the Open Access version, provided by the Computer Vision Foundation.
Except for this watermark, it is identical to the accepted version;
the final published version of the proceedings is available on IEEE Xplore.

Damage Detection and Localization by Learning Deep Features of Elastic Waves in Piezoelectric Ceramic Using Point Contact Method

Pragyan Banerjee[1] Pranjal Saxena[1] Nur M M Kalimullah[1] Amit Shelke[1] Anowarul Habib[2]
[1]Indian Institute of Technology Guwahati, India
[2]UiT The Arctic University of Norway
[1]{firstname.lastname}@iitg.in [2]{firstname.lastname}@uit.no

Abstract

The reliable detection and localization of damages in piezoelectric materials such as Lead Zirconate Titanate (PZT) pose significant challenges in various engineering applications. Conventional methods for damage detection often depend on manual inspection or basic signal processing techniques, which are subjective, labor-intensive, and susceptible to human error. In this paper, a novel approach for damage detection and localization in PZT materials using deep learning techniques is proposed. Leveraging a convolutional neural network (CNN) in tandem with methodologies such as class activation mapping (CAM), the objective is to enhance the accuracy and reliability of fault detection systems. In particular, the VGG16 architecture is adopted as the foundation of the proposed framework due to its simplicity and effectiveness in large-scale image recognition tasks. By integrating CAM into the training process, CNNs are equipped to precisely localize anomalies within PZT ceramic images, facilitating improved fault detection performance. The study demonstrates the effectiveness of deep learning methods in addressing the challenges of fault detection and localization in PZT materials, offering promising avenues for advancing monitoring and maintenance practices in various engineering applications.

1. Introduction

Lead Zirconate Titanate (PZT) ceramics are essential in numerous industrial and military applications. They contribute to optoelectronics, telecommunication, biomedical devices, actuators, energy harvesting devices, and structural health monitoring (SHM) [1, 5, 20, 25, 37]. Acoustic transducers, which also utilize piezoelectric materials, have experienced rapid adoption and found applications in diverse fields, ranging from medical diagnosis to industrial testing and quality control [8, 19]. Conversely, the broad application of ultrasound imaging in various fields stems from its manifold advantages, including its affordability and its capacity to gather information without causing damage or requiring invasive procedures. The precise localization and detection of damage at the micro-scale are crucial aspects of ultrasonic-based SHM. The effectiveness of piezoelectric sensors significantly influences the accuracy and consistency of the diagnosis. Continuous use of the sensor, particularly in environments with humidity, temperature fluctuations, and corrosive conditions, may lead to its degradation.

Surface or subsurface flaws can also be inherent to the bulk material, occasionally introduced during the final stages of fabrication or the early phases of device operation. Near-surface flaws hold particular significance for various applications, given that operational stresses often concentrate around the periphery of these defects. Both bulk and surface microscale defects in PZT ceramics serve as precursors to damage, imposing limitations on the strength, lifespan, and performance of the sensors [9]. Before installation, it is imperative to calibrate and compensate all sensors for errors and disturbances resulting from harsh environmental conditions and temperature fluctuations. Measurement errors can arise due to minor defects in degraded sensors, and these are typically addressed by adjusting the acquired responses using a baseline compensation factor. Immediately post-installation, sensors are assumed to be in a healthy state, but ongoing efforts should be dedicated to periodic assessments and monitoring of sensor health. However, a sensor with micro-scale cracks exhibits higher-order effects and nonlinear piezoelectric behavior, discouraging the use of simplified compensation factors. Hence, detecting, localizing, and quantifying defects in the piezo ceramic becomes crucial to prevent false alarms in SHM applications.

In recent decades, significant efforts have been directed toward developing innovative nondestructive evaluation (NDE) techniques for detecting surface and internal damage in ceramic components [9,29,40]. Alongside ultrasonic imaging, various optical methods have characterized surface defects in PZT ceramics. Common optical measure-

ments include photoacoustic microscopy, optical coherence tomography, and optical gating techniques [4, 34, 39, 40]. PZT ceramics exhibit high scattering behavior at optical wavelengths, resulting in noisy measurements [3]. Recently, a scanning laser Doppler vibrometer (SLDV) has been used to visualize acoustic wave interference with inclusions and damages in metallic plates, piezo-ceramics, and piezo-crystals in three dimensions [17, 32]. However, SLDV experiments are costly and require a thin reflective coating on the sample surface.

2. Relation to prior work

This study expands the point contact method (Coloumb coupling) to observe the interaction of ultrasonic waves with surface anomalies in sintered piezoelectric substrates. A steel sphere probe serves as a Coulomb electrode for exciting and detecting ultrasonic waves. These Waves experience reflections, interferences, and mode conversions when encountering defects and material boundaries, leading to spatial and temporal dispersion. Localizing and quantifying defects from wave visualization in such scenarios pose challenges, emphasizing the need to extract damage-sensitive features from the collected experimental data.

Neural networks (NNs), the foundational architecture of deep learning, find widespread application across diverse scientific and engineering domains [6, 14, 30, 35]. The inaugural NN model, Neocognitron [10], shares key features with contemporary deep neural networks, including multilayer structures, max pooling, convolution, and non-linear dynamics. Notably, the universal approximation theorem assures that an NN with sufficient hidden units and linear output can effectively represent any arbitrary function or dataset, including intricate waveform data [7, 15, 16]. A key advantage of deep learning lies in its ability to hierarchically extract features from data, thereby accurately approximating functions without the need for manual feature selection or predefined user bases [11, 24].

Deep learning has garnered considerable attention in scientific computing and offers numerous avenues for advancing SHM. Deep learning methodologies are extensively utilized for diagnosing civil and mechanical structures, yielding promising outcomes [22, 26, 27, 36]. Neural networks, alongside other deep learning frameworks, are employed to detect anomalies in composite structures through vibration and frequency-based techniques [2, 23]. Several studies leverage guided waves in tandem with deep learning architectures for damage detection in composite structures [31, 33]. Moreover, Melville et al. (2018) employ classical machine learning techniques such as support vector machines (SVM) and deep learning algorithms for anomaly detection in full wavefield images [28]. These images are captured using piezoelectric actuators and a laser Doppler vibrometer. Deep learning methods demonstrate superior performance in damage detection compared to SVM-based approaches. Zhou et al. introduced class activation mapping (CAM) utilizing CNN feature maps to precisely localize objects within images [41]. By integrating CAM into the training process, CNNs can effectively identify relevant features within images.

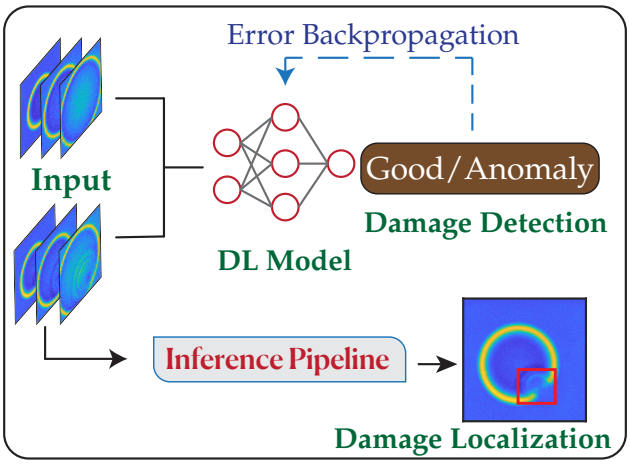

Figure 1. The figure illustrates the overall flow of the proposed method. The dataset is utilized to train the model for binary classification. Following the model training, the inference pipeline is employed to create the bounding boxes.

Additionally, Simonyan and Zisserman introduced the VGG16 architecture, renowned for its simplicity and remarkable performance in image recognition [38]. VGG16's uniform configuration and deep architecture enable efficient training and hierarchical feature learning from raw image data. Leveraging insights from these works, our research builds upon CNN strengths for fault detection and localization in PZT materials.

3. Materials and method

The proposed method for damage detection, as shown in the Fig. 1, leverages the power of transfer learning by utilizing the VGG16 convolutional neural network architecture pre-trained on the ImageNet dataset. In our approach, we adapt the VGG16 model by replacing the conventional flattening and dense layers with a global average pooling layer followed by a single dense layer. By fine-tuning the adapted VGG16 model on our dataset, we aim to achieve robust and accurate detection of damage in various industrial and medical imaging applications.

In addition to adapting the VGG16 model architecture for fault detection, we employ a technique utilizing heat maps generated from the feature maps to generate bounding boxes around detected damage. After passing an image through the adapted VGG16 model, feature maps are extracted from intermediate convolutional layers. These fea-

ture maps capture rich spatial information corresponding to different aspects of the input image. Heat maps are generated to highlight regions of the image that contribute most significantly to the model's classification decision. Subsequently, thresholding is used to localize and refine the regions of interest, thereby generating bounding boxes around detected damage. This approach enables precise localization of damage within images, facilitating further analysis and decision-making in fault detection applications.

3.1. Experimental dataset

To aid in the development and assessment of fault detection and localization methods, we employed a carefully crafted dataset comprised of spatiotemporal data matrices obtained through coulomb coupling imaging. Each dataset entry consists of a 365 matrices with dimensions of 200×200, capturing both spatial and temporal features. The spatial aspect of each snapshot is represented by 200×200 pixels, equivalent to a physical area of 10 millimeters by 10 millimeters. Our dataset was meticulously gathered over a total acquisition time of 1 microsecond, resulting in 4000 time-varying snapshots. Interestingly, these snapshots exhibit a repeating pattern approximately every 365 frame, reflecting the cyclic nature of the observed waves due to experimental conditions. To ensure a comprehensive dataset, we included only one complete cycle of 365 images, each representing distinct wave patterns essential for analysis and model training. We used two such types of images-good and anomaly, resulting in 730 images. The images were normalised prior to feeding into the model. We train the model using our dataset using a learning rate of 0.0001 with a batch size of 10, for 10 epochs using Adam optimizer.

3.2. Experimental setup

The experimental setup for point contact excitation and detection is depicted in Fig. 2. This state-of-the-art experimental technique, based on the Coulomb coupling method, facilitates the excitation and detection of ultrasonic waves in piezoelectric materials [21]. The transformation of electromagnetic energy to acoustic energy in piezoelectric materials is governed by the electric field gradient and piezoelectric properties gradient through Coulomb coupling. The technique involves generating an electric field to induce stress waves via electromechanical excitation [12, 13, 18]. The excitation Dirac delta pulse with a time width of 70 ns was generated by an arbitrary function generator (Agilent 81150A). The generated signal is delivered for amplification through a radio-frequency (RF) amplifier (AMP018032-T). Subsequently, these amplified signals were directed to the excitation steel probe, which gently contacted the surface of the PZT sample. The induced acoustic waves in the specimen were then acquired using a similar steel probe on the opposite surface of the

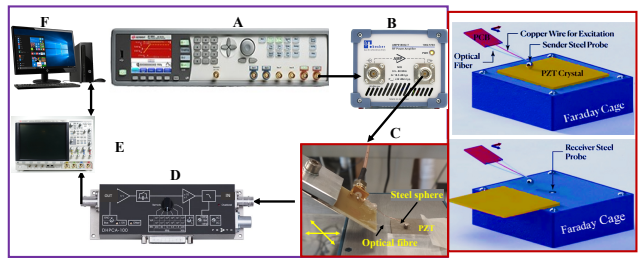

Figure 2. A schematic diagram represents the experimental configuration for point contact excitation and detection. Signal generation (Block A) amplifies the signal (Block B), initiating acoustic waves in the Coulomb probe configuration (Block C). Transimpedance conversion (Block D) directs signals to the oscilloscope (Block E) for averaging and digitization. Following this, data is transferred via USB to a PC (Block F). The image acquisition area covered 10 mm × 10 mm, with a step size of 50 μm in both directions.

PZT. The ultrasonic waves were amplified using a transimpedance amplifier (DHPCA-100), converting current to voltage with adjustable amplification. The amplified signal was then captured by an oscilloscope (Agilent 3024A) with 12-bit digitization capability and a sampling interval of 25 ns. The oscilloscope averaged 256 pulse shots, and the digitized signal was stored in a PC via USB. The PC controlled the XY plane mechanical scanner, covering a scanning area of $10\,mm \times 10\,mm$ with a step size of 50 μm in both directions. The experiment aims to visualize the spatial-temporal evolution of ultrasonic waves in a PZT sample for anomaly identification. Initially, a healthy PZT specimen is placed in the setup, and Coulomb scanning is conducted. Controlled surface damage is then introduced using a diamond drill after the scanning process.

3.3. Model Architecture

In this section, a detailed description is presented of the modified VGG16 convolutional neural network architecture utilized for damage detection using binary image classification. The modified VGG16 architecture, which can be clearly seen in Fig. 3, consists of 5 convolutional blocks, denoted as B_1 through B_5. Each convolutional block comprises stacked convolutional layers, followed by max-pooling layers for spatial downsampling. Mathematically, the output of the i-th convolutional block B_i is represented as follows:

$$X_i = \text{Conv}_i(X_{i-1}) \quad \text{for} \quad i = 1, 2, 3, 4, 5 \tag{1}$$

Where X_0 represents the input image, X_{i-1} represents the input feature map to the ith convolutional block, Conv_i denotes the set of convolutional layers within the ith block, and X_i denotes the output feature map of the ith convolutional block.

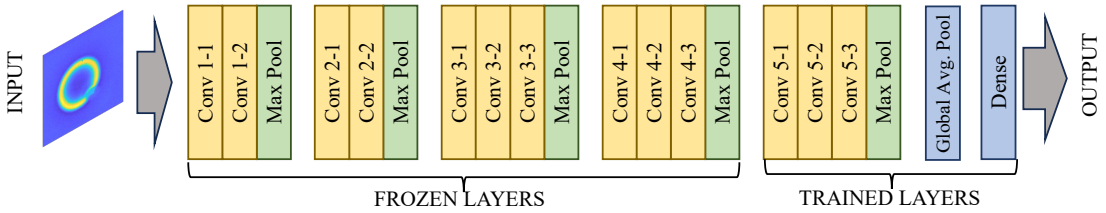

Figure 3. This image represents the architecture of a custom multi-class classification model built with a VGG16 feature extractor and a custom classification head. The model is pre-trained on ImageNet and parameters for the first convolutional blocks are frozen. The model returns class scores when in train mode and class probabilities and normalized feature maps when in evaluation mode.

After the final convolutional block, the output feature map X_5 undergoes global average pooling to aggregate spatial information across each feature map. Mathematically, global average pooling computes the average value of each feature map, yielding a fixed-length feature vector. The global average pooling operation is represented as:

$$Y = \frac{1}{h \times w} \sum_{i=1}^{h} \sum_{j=1}^{w} X_5(i,j) \tag{2}$$

Where, Y represents the output of the global average pooling operation, h and w denote the height and width of the feature map X_5, respectively, and $X_5(i,j)$ represents the activation value at position (i,j) in the feature map X_5. Following global average pooling, the fixed-length feature vector Y is fed into a single dense layer acting as the classification head. The dense layer consists of neurons corresponding to the 2 output classes and employs the softmax activation function to produce class probabilities. Mathematically, the output of the dense layer Z is computed as:

$$Z = \text{Softmax}(W_{\text{dense}} \cdot Y + b_{\text{dense}}) \tag{3}$$

Where W_{dense} and b_{dense} denote the weight matrix and bias vector of the dense layer, respectively. The first 4 convolutional blocks based on the VGG 16 network pre-trained on the ImageNet dataset are frozen. The last convolutional block and the dense layer are then fine-tuned on our dataset.

3.4. Method to generate bounding boxes

During inference, our objective extends beyond mere image classification to include the localization of anomalies by generating bounding boxes around detected defects. As shown in Fig. 4, this process involves leveraging the model's inference mode to output both class probabilities and heat maps, which are subsequently processed to derive bounding boxes.

Let $F = \{F_1, F_2, ..., F_{512}\}$ denote the set of feature maps extracted from the Conv5–3 layer, each with dimensions 14×14. Each feature map F_i highlights distinct regions in the input image I. Leveraging the architecture's

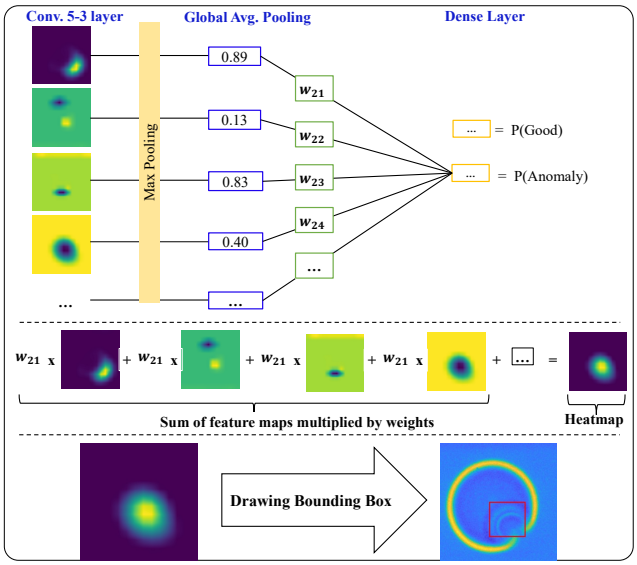

Figure 4. This image shows how a CNN detects anomalies in images. It transforms feature maps into heat maps, highlighting anomalous regions. The process includes global average pooling, a dense layer for probability calculation, and the multiplication of feature maps with weights. Detected anomalies are marked with bounding boxes on the heatmap.

Global Average Pooling Layer and Dense Layer, we ascertain the influence of each feature map on the classification scores, particularly the 'Anomaly' class. Let $W_{\text{dense}} = \{w_1, w_2, ..., w_{512}\}$ denote the weights of the Dense Layer corresponding to each feature map. The weighted sum of feature maps is computed as:

$$H = \sum_{i=1}^{512} w_i \cdot F_i \tag{4}$$

The generated heat map H is upsampled to match the input image's size of 224×224. Bilinear upsampling is employed for this purpose, ensuring the preservation of spatial relationships. The heat map H is normalized using the following equation:

$$H_{\text{norm}}(x, y) = \frac{H(x, y) - \min(H)}{\max(H) - \min(H)} \tag{5}$$

A threshold θ is selected to segment the heat map, transforming values exceeding the threshold to 1 and those below 0:

$$H_{\text{binarized}}(x, y) = \begin{cases} 1 & \text{if } H_{\text{norm}}(x, y) \geq \theta \\ 0 & \text{otherwise} \end{cases} \tag{6}$$

The segmented regions represented by 1s in the heatmap $H_{\text{binarized}}$ are considered as contiguous dense regions. Bounding box B are generated around these contiguous regions by identifying the minimum and maximum values along the height and width dimensions, and their coordinates are given by:

$$(x_{\text{min}}, y_{\text{min}}), (x_{\text{max}}, y_{\text{min}}), (x_{\text{max}}, y_{\text{max}}), (x_{\text{min}}, y_{\text{max}}) \tag{7}$$

However, the size of the bounding box is affected by the threshold value.

4. Results and discussion

The method is tested on two factors: the model's performance as a binary classifier and its performance on damage localization.

4.1. Evaluation Metrics

To assess the classification performance of our damage detection model, we employ a comprehensive set of evaluation metrics, including accuracy, balanced accuracy, precision, recall, and F1 score. To evaluate the model's performance on damage localization, we employ a systematic procedure involving the division of the image into four quadrants and a comparison of the bounding box centroids within these quadrants which is evident in the Fig. 5. Let I represent the input image, B denote the bounding box, and $C(B)$ represent the centroid of the bounding box B.

Beginning by dividing the image I into four quadrants, denoted as Q_1, Q_2, Q_3, and Q_4, with the origin at the center of the image. Each quadrant Q_i is defined by its respective coordinate ranges, where $i = 1, 2, 3, 4$. Ideally, due to the isotropic nature of acoustic wave propagation in the PZT material, all quadrants should exhibit symmetry.

Next, calculate the centroid $C(B)$ of the bounding box B detected within the image I. Subsequently, determining the quadrant Q_B containing the centroid $C(B)$ of the bounding box B.

Following this, pairwise comparisons of all the quadrants Q_i are performed in terms of Structural Similarity Index (SSIM) to identify the quadrant with the lowest average SSIM with the other quadrants. Let Q_A represent this quadrant.

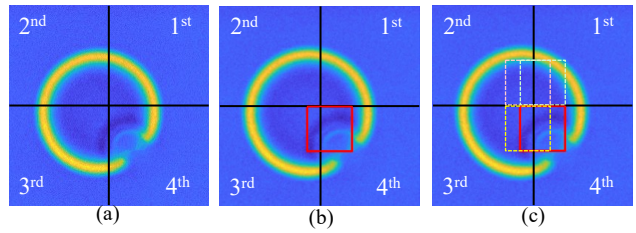

Figure 5. This image illustrates the process of evaluating a model's performance. It involves dividing the image into four quadrants, comparing bounding box centroids within these quadrants, and using metrics such as accuracy. The process is part of a comprehensive assessment of the model's effectiveness in localizing damages within identified quadrants.

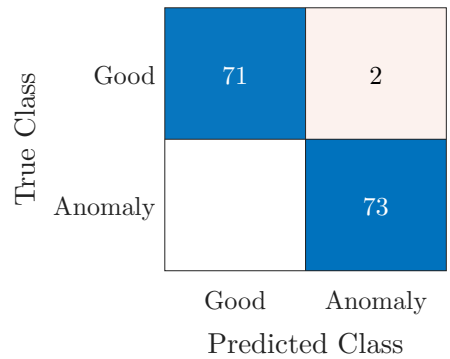

Figure 6. The confusion matrix shows the classification model's performance. It correctly predicted 71 "Good" and 73 "Anomaly", with only 2 "Anomaly" misclassified as "Good". No "Good" was misclassified as an "Anomaly".

Finally, we compute accuracy between quadrants Q_A and Q_B for all the images in the test set, considering the classification of damage localization within these regions. This evaluation metric provides a comprehensive assessment of the model's performance in localizing damages within the identified quadrants, as evident in Fig. 6 facilitating the evaluation of damage detection accuracy and effectiveness in practical applications.

4.2. Quantitative analysis

We tested our method across the different aforementioned metrics and got the following results. The value of θ is a hyper-parameter in our method and can be chosen according to the use case. We studied how the accuracy of choosing the correct quadrant of the bounding box depends on the value of θ in Fig. 7. In the study, exploration was conducted on the performance of ten distinct models, each characterized by its unique architecture. Primarily, three loss functions were utilized: Cross Entropy (Original Loss Function), Negative Log Likelihood (NLL), and Multi-Margin Loss (MML). From these loss functions,

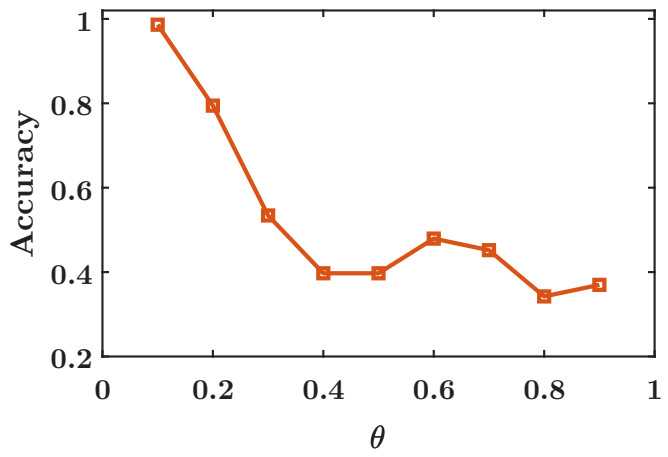

Figure 7. The plot shows the relationship between the accuracy of a model and the hyperparameter θ. This shows the dependence on choosing the right value of hyper-parameter in determining the performance of the model.

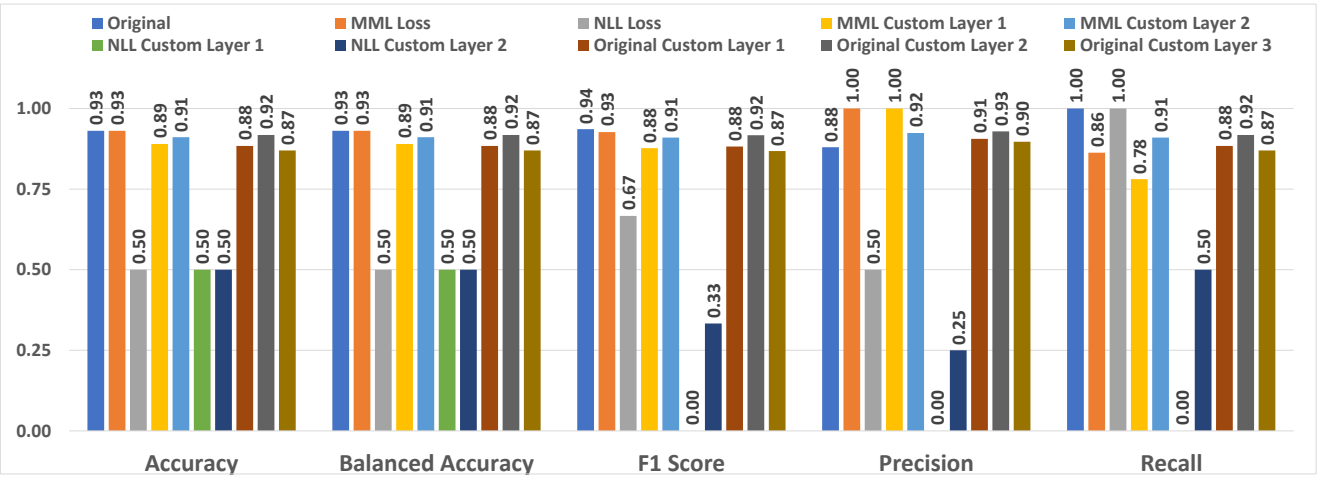

Figure 8. The figure illustrates the performance of ten different models using various loss functions and layers, evaluated against some widely used metrics named Accuracy, Balanced Accuracy, Precision, F1 Score, and Recall, using the same dataset.

ten models with varying layers were created. The layers employed included: Custom Layer 1 maintains the architecture of the Original Model while modifying the forward method. Custom Layer 2 simplifies the classifier attribute of the Original Model. The new classifier is a sequential model comprising a linear layer that accepts 4096 inputs and produces 2048 features, followed by a ReLU activation function, a dropout layer with a dropout rate of 0.5, and a final linear layer that accepts 2048 inputs and yields 10 features.

The third layer type, Custom Layer 3, is a modification of the Original Model. The classifier attribute of the model is altered to include a sequential model with a linear layer that accepts 4096 inputs and produces 2048 features, followed by a ReLU activation function, a dropout layer with a dropout rate of 0.5, an additional linear layer that accepts 2048 inputs and yields 1024 features, another ReLU activation function, another dropout layer with a dropout rate of 0.5, and a final linear layer that accepts 1024 inputs and yields 10 features. Using these layers, ten models were formed: Original, Original Custom Layer 1, Original Custom Layer 2, Original Custom Layer 3, MML Loss (where only the loss function was changed but the layers in the model remained the same as the Original), MML Custom Layer 1, MML Custom Layer 2, NLL Loss (where the loss function was changed but the layers in the model remained the same as the Original), NLL Custom Layer 1, and NLL Custom Layer 2.

After evaluating the performance of all the models using widely used metrics such as Accuracy, Balanced Accuracy, Precision, F1 Score, and Recall, in Fig. 8 it was found that the Original Model outperformed the others. The efficiency

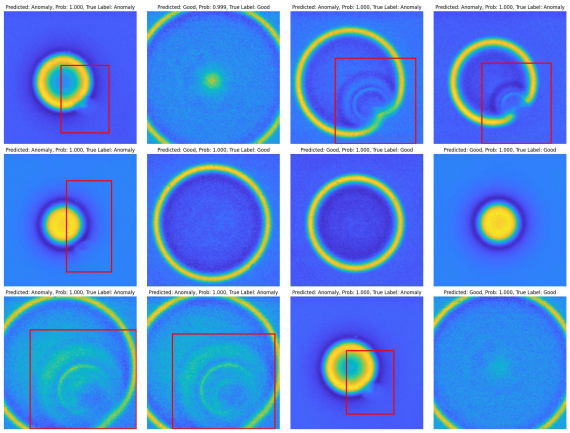

Figure 9. The figure illustrates the performance of the original model in the classification task in predicting whether the image is good or an anomaly with respect to the true label. It also represents the probability and the location of the bounding box formed.

of this model can also be seen in Fig. 9 which represents its capabilities in predicting the labels correctly and forming the best-suited bounding box.

5. Conclusion

A novel experimental technique based on Coulomb coupling is employed to visualize the spatial-temporal evolution of ultrasonic waves in the PZT sensor. Sequential temporal signals of the excited ultrasonic wave in the PZT are analyzed to detect and quantify surface defects. This study emphasizes the effectiveness of utilizing deep learning methods, particularly CNNs, for detecting and locating the damage in the PZT ceramics. Through the incorporation of techniques such as class activation mapping (CAM) and the utilization of architectures like VGG16, the study has demonstrated enhanced accuracy and reliability in the detection of anomalies within images of PZT materials. CAM enables localization of the areas in the image that contribute most significantly to the model's classification decision while leveraging the VGG16 architecture to provide a robust framework for feature extraction and anomaly identification within the PZT material images. These results emphasize the capacity of deep learning methods to improve damage detection systems, facilitating more resilient and effective monitoring and maintenance of PZT-based devices and structures. Future investigations in this field offer the prospect of enhancing fault detection techniques and extending their utility across diverse engineering disciplines.

6. Acknowledgement

This work was supported by the Research Council of Norway, Cristin Project, ID: 2061348.

References

[1] V Agarwal, A Shelke, BS Ahluwalia, F Melandsø, T Kundu, and A Habib. Damage localization in piezo-ceramic using ultrasonic waves excited by dual point contact excitation and detection scheme. *Ultrasonics*, 108:106113, 2020. 1

[2] Hyun-Tae Bang, Solmoi Park, and Haemin Jeon. Defect identification in composite materials via thermography and deep learning techniques. *Compos. Struct.*, 246:112405, 2020. 2

[3] M Bashkansky, MD Duncan, M Kahn, D Lewis, and J Reintjes. Subsurface defect detection in ceramics by high-speed high-resolution optical coherent tomography. *Optics Letters*, 22(1):61–63, 1997. 2

[4] Philip R Battle, Mark Bashkansky, Rita Mahon, and John F Reintjes. Subsurface defect detection in ceramic materials using optical gating techniques. *Optical Engineering*, 35:1119–1123, 1996. 2

[5] Suresh Bhalla and Chee Kiong Soh. Structural health monitoring by piezo-impedance transducers. i: Modeling. *J. Aerosp. Eng.*, 17(4):154–165, 2004. 1

[6] William Bort, Igor I Baskin, Timur Gimadiev, Artem Mukanov, Ramil Nugmanov, Pavel Sidorov, Gilles Marcou, Dragos Horvath, Olga Klimchuk, Timur Madzhidov, et al. Discovery of novel chemical reactions by deep generative recurrent neural network. *Sci. Rep.*, 11(1):3178, 2021. 2

[7] George Cybenko. Approximation by superpositions of a sigmoidal function. *Mathematics of control, signals and systems*, 2(4):303–314, 1989. 2

[8] Pengfei Du, Weishan Chen, Jie Deng, Shijing Zhang, Junjie Zhang, and Yingxiang Liu. A critical review of piezoelectric ultrasonic transducers for ultrasonic-assisted precision machining. *Ultrasonics*, page 107145, 2023. 1

[9] Michael D Duncan, Mark Bashkansky, and John Reintjes. Subsurface defect detection in materials using optical coherence tomography. *Opt. Express*, 2(13):540–545, 1998. 1

[10] Kunihiko Fukushima, Sei Miyake, and Takayuki Ito. Neocognitron: A neural network model for a mechanism of visual pattern recognition. *IEEE Trans. Syst. Man Cybern.: Syst.*, (5):826–834, 1983. 2

[11] Ian Goodfellow, Yoshua Bengio, and Aaron Courville. *Deep learning*. MIT press, 2016. 2

[12] A Habib, A Shelke, M Pluta, U Pietsch, T Kundu, and W Grill. Scattering and attenuation of surface acoustic waves and surface skimming longitudinal polarized bulk waves imaged by coulomb coupling. In *AIP Conference Proceedings*, volume 1433, pages 247–250. A. I. P, 2012. 3

[13] A Habib, E Twerdowski, M von Buttlar, M Pluta, M Schmachtl, R Wannemacher, and W Grill. Acoustic holography of piezoelectric materials by coulomb excitation. In *Health Monitoring and Smart Nondestructive Evaluation of Structural and Biological Systems V*, volume 6177, pages 383–390. SPIE, 2006. 3

[14] Allard A Hendriksen, Minna Bührer, Laura Leone, Marco Merlini, Nicola Vigano, Daniël M Pelt, Federica Marone, Marco Di Michiel, and K Joost Batenburg. Deep denoising for multi-dimensional synchrotron x-ray tomography with-

out high-quality reference data. *Sci. Rep.*, 11(1):11895, 2021. 2

[15] Kurt Hornik, Maxwell Stinchcombe, and Halbert White. Multilayer feedforward networks are universal approximators. *Neural networks*, 2(5):359–366, 1989. 2

[16] Kurt Hornik, Maxwell Stinchcombe, and Halbert White. Universal approximation of an unknown mapping and its derivatives using multilayer feedforward networks. *Neural networks*, 3(5):551–560, 1990. 2

[17] Zhaorong Huang, Qi Zhang, Silvana Corkovic, Robert Dorey, and Roger W Whatmore. Comparative measurements of piezoelectric coefficient of pzt films by berlincourt, interferometer, and vibrometer methods. *IEEE Trans. Ultrason. Ferroelectr. Freq. Control*, 53(12):2287–2293, 2006. 2

[18] S Jadhav, R Kuchibhotla, Krishna A, A Habib, and Dilip K Prasad. Deep learning-based denoising of acoustic images generated with point contact method. *Journal of Nondestructive Evaluation, Diagnostics and Prognostics of Engineering Systems*, 6(3), 2023. 3

[19] Licheng Jia, Lei Shi, Chongbin Liu, Jing Xu, Yongjie Gao, Chengliang Sun, Sheng Liu, and Guoqiang Wu. Piezoelectric micromachined ultrasonic transducer array-based electronic stethoscope for internet of medical things. *IEEE Internet Things J.*, 9(12):9766–9774, 2022. 1

[20] Zheng Jiang, Robert J Dickinson, Timothy L Hall, and James J Choi. A pzt–pvdf stacked transducer for short-pulse ultrasound therapy and monitoring. *IEEE Trans. Ultrason. Ferroelectr. Freq. Control*, 68(6):2164–2171, 2021. 1

[21] Nur MM Kalimullah, A Shelke, and A Habib. A deep learning approach for anomaly identification in pzt sensors using point contact method. *Smart Mater. Struct.*, 32(9):095027, 2023. 3

[22] Nur M-M Kalimullah, A Shelke, and A Habib. A probabilistic framework for source localization in anisotropic composite using transfer learning based multi-fidelity physics informed neural network (mfpinn). *Mech. Syst. Signal Process.*, 197:110360, 2023. 2

[23] Asif Khan, Dae-Kwan Ko, Soo Chul Lim, and Heung Soo Kim. Structural vibration-based classification and prediction of delamination in smart composite laminates using deep learning neural network. *Composites, Part B*, 161:586–594, 2019. 2

[24] Yann LeCun, Yoshua Bengio, and Geoffrey Hinton. Deep learning. *nature*, 521(7553):436–444, 2015. 2

[25] Tao Li and Pooi See Lee. Piezoelectric energy harvesting technology: from materials, structures, to applications. *Small Struct.*, 3(3):2100128, 2022. 1

[26] Yi-zhou Lin, Zhen-hua Nie, and Hong-wei Ma. Structural damage detection with automatic feature-extraction through deep learning. *Comput.-Aided Civ. Infrastruct. Eng.*, 32(12):1025–1046, 2017. 2

[27] Z Liu, Y Cao, Y Wang, and W Wang. Computer vision-based concrete crack detection using u-net fully convolutional networks. *Autom. Constr.*, 104:129–139, 2019. 2

[28] Joseph Melville, K Supreet Alguri, Chris Deemer, and Joel B Harley. Structural damage detection using deep learning of ultrasonic guided waves. In *AIP conference proceedings*, volume 1949. AIP Publishing, 2018. 2

[29] Hongchen Miao and Faxin Li. Shear horizontal wave transducers for structural health monitoring and nondestructive testing: A review. *Ultrasonics*, 114:106355, 2021. 1

[30] Cheng Peng, Yufeng Chen, Weihua Gui, Zhaohui Tang, and Changyun Li. Remaining useful life prognosis of turbofan engines based on deep feature extraction and fusion. *Sci. Rep.*, 12(1):6491, 2022. 2

[31] Cheng Qian, Yunmeng Ran, Jingjing He, Yi Ren, Bo Sun, Weifang Zhang, and Rongqiao Wang. Application of artificial neural networks for quantitative damage detection in unidirectional composite structures based on lamb waves. *Adv. Mech. Eng.*, 12(3):1687814020914732, 2020. 2

[32] Lifeng Qin, Yingying Sun, Qing-Ming Wang, Youliang Zhong, Ming Ou, Zhishui Jiang, and Wei Tian. Fabrication and characterization of thick-film piezoelectric lead zirconate titanate ceramic resonators by tape-casting. *IEEE Trans. Ultrason. Ferroelectr. Freq. Control*, 59(12):2803–2812, 2012. 2

[33] Mahindra Rautela and S Gopalakrishnan. Ultrasonic guided wave based structural damage detection and localization using model assisted convolutional and recurrent neural networks. *Expert Syst. Appl.*, 167:114189, 2021. 2

[34] Armando Reyes-Montero, Fernando Rubio-Marcos, Luis Edmundo Fuentes-Cobas, Adolfo Del Campo, Rosalba Castaneda-Guzman, María Elena Villafuerte-Castrejón, and Lorena Pardo. Confocal raman microscopy, synchrotron x-ray diffraction, and photoacoustic study of ba0. 85ca0. 15ti0. 90zr0. 10o3: understanding structural and microstructural response to the electric field. *ACS Appl. Electron. Mater.*, 3(7):2966–2976, 2021. 2

[35] A Sagheer and M Kotb. Unsupervised pre-training of a deep lstm-based stacked autoencoder for multivariate time series forecasting problems, sci. rep., 9: 19038, 2019, 2019. 2

[36] Haidong Shao, Hongkai Jiang, Huiwei Zhao, and Fuan Wang. A novel deep autoencoder feature learning method for rotating machinery fault diagnosis. *Mech. Syst. Signal Process.*, 95:187–204, 2017. 2

[37] Jung Ho Shin, Young B Kim, Jung Hwan Park, Jin Soo L, Sang Hyun Park, Seung Hyung L, Jae Hee Lee, and Keon J Lee. Light-material interfaces for self-powered optoelectronics. *J. Mater. Chem. A*, 9(46):25694–25705, 2021. 1

[38] Karen Simonyan and Andrew Zisserman. Very deep convolutional networks for large-scale image recognition. *arXiv preprint arXiv:1409.1556*, 2014. 2

[39] Rong Su, Mikhail Kirillin, Ernest W Chang, Ekaterina Sergeeva, Seok H Yun, and Lars Mattsson. Perspectives of mid-infrared optical coherence tomography for inspection and micrometrology of industrial ceramics. *Opt. Express*, 22(13):15804–15819, 2014. 2

[40] Zhike Zhao. Review of non-destructive testing methods for defect detection of ceramics. *Ceram. Int.*, 47(4):4389–4397, 2021. 1, 2

[41] Bolei Zhou, Aditya Khosla, Agata Lapedriza, Aude Oliva, and Antonio Torralba. Learning deep features for discriminative localization. In *Proceedings of the IEEE conference on computer vision and pattern recognition*, pages 2921–2929, 2016. 2